

Types of Size-Dependent Melting in Fe Nanoclusters: a Molecular Dynamics Study

Louis E. S. Hoffenberg, Alexander Khrabry,^{a)} Yuri Barsukov,^{b)} Igor D. Kaganovich,^{b)} and David B. Graves^{c)}
*Department of Chemical and Biological Engineering, Princeton University, Princeton,
 New Jersey 08540*

(Dated: November 19, 2024)

Metallic nanoclusters are of interest in many fields because of their size-dependent catalytic activity. This activity can, in part, be influenced by their melting properties. In this work, the melting phase transitions of Fe_n nanoclusters with $n \leq 100$ atoms were investigated using classical many-body molecular dynamics simulations. Adding a single atom to many cluster sizes induced strong variations in surface and core melting points, and cluster energetics. Clusters with size-dependent melting behavior were classified into 3 distinct cluster types: closed-shell, near-closed-shell, and far-from-closed-shell clusters. For small clusters, near-closed-shell clusters had very low surface melting points and very high melting points (heat capacity maximum). Cluster sizes with symmetric closed shells and near-closed shells almost always had first-order-like phase transitions. For intermediate cluster sizes, far-from-closed-shell clusters often exhibited second-order-like phase transitions due to geometric factors. Larger cluster sizes began to favor bcc lattice structures. Variations in the surface and core melting behavior of neighboring cluster sizes may have implications for catalytic systems such as the growth of single-wall carbon nanotubes.

I. INTRODUCTION

Nanoparticles (NPs) – i.e., particulate material with characteristic dimensions under 100 nm – have interesting properties that make them desirable for catalytic^{1,2}, optoelectronic³, and biomedical⁴ applications, among many others. These properties can depend on many factors like nanoparticle size, composition, degree of crystallinity, and other structural elements. The phase of the NP can have a significant effect on properties since atoms in liquid particles have considerably more mobility than in solid form. For example, it has been proposed that carbon nanotube (CNT) growth on catalytic iron NPs depends in part on carbon precursor adsorption, surface diffusion, and dissolution into the NP^{5,6} – all of which can be influenced by the NP phase⁷. The transition between solid and liquid NP phases is therefore of potential importance in multiple applications.

The melting points for NPs are known to differ from those of their corresponding bulk materials^{8–10}. NP melting temperatures are lower than the bulk melting point due to larger surface-atom-to-volume-atom ratios¹¹. Surface atoms are bonded to fewer atoms than the inner atoms, so smaller NPs require less energy to melt than larger ones. Their melting points scale according to the Gibbs-Thomson equation:

$$T_{m,NP} = T_{m,bulk} \left(1 - 2 \frac{\sigma_{sl}}{\Delta H_m \rho_s r} \right) \quad (1)$$

where σ_{sl} is the solid-liquid interfacial energy, ΔH_m is

the bulk latent heat of the melting, ρ is the bulk solid density, and r is the radius of the NP¹².

It is also known that when the NP radius is below some threshold size range (i.e., approaching the nanocluster regime), melting points no longer follow the Gibbs-Thomson equation. Instead, melting temperatures can fluctuate strongly with cluster size, with the addition or subtraction of a single atom. Sometimes, the nanocluster melting points can exceed those of the bulk solid¹³.

This variation in melting points is attributed to interrelated geometric and electronic quantum size effects^{14–16}, collectively called magic number effects. Magic number *clusters* are nanoclusters with particularly stable structures due to either configurational symmetry that maximizes bonding between atoms (corresponding to geometric magic numbers) or electronic effects that stabilize certain cluster geometries (i.e., electronic magic numbers)^{14–16}. Magic numbers have been documented to affect melting behavior and the Gibbs free energies of formation for small metal clusters^{17,18}.

In larger systems and NPs, atoms are frequently approximated as *surface* or *bulk*. The transition regime between Gibbs-Thomson NP scaling and the nanocluster fluctuation regime is thought to occur when the cluster's atoms can no longer fit the surface-bulk binary¹⁹. When clusters fall in this regime, there are fewer bulk atoms and distinct *types* of surface atoms with different binding energies, which determine cluster energetics. Because certain structures have perfectly closed atomic shells (geometric magic numbers)²⁰, nanoclusters with more or fewer atoms have notably different binding energies per atom and therefore different melting temperatures^{15,16,21}. Ion calorimetry measurements of Al nanoclusters have revealed that the transition between Gibbs-Thomson NP scaling and nanocluster variation of melting temperatures occurs between clusters of 150 and 342 atoms²². Simulations of Ni nan-

^{a)}Andlinger Center for Energy and the Environment, Princeton University, Princeton, New Jersey 08540

^{b)}Princeton Plasma Physics Laboratory, Princeton, New Jersey 08540

^{c)}Electronic mail: dgraves@princeton.edu

oclusters observed the Gibbs-Thompson NP scaling in clusters as small as 90 atoms²³.

The nanocluster size range, which is the focus of this work, is particularly interesting for some catalysis applications such as the catalytic growth of carbon nanotubes with Fe or Fe-containing alloys in floating catalyst chemical vapor deposition (FCCVD)^{7,24}. Fe nanoclusters of up to ~ 100 atoms (~ 1.2 nm in diameter) are most relevant to the growth of single-wall CNTs (SWCNTs)⁷. This work focuses on Fe nanoclusters. Despite interest in iron nanoparticles for the catalytic growth of CNTs, among other applications, the melting behavior of Fe nanoclusters has garnered few dedicated studies^{25–27}. Furthermore, no study has analyzed the majority of the Fe nanocluster size range. The caloric curves describing Fe cluster melting behavior in this work are used in the accompanying paper²⁸ to determine the free energies of cluster formation in the kinetic modeling of nucleation and growth from condensing vapor.

The process of melting in nanoclusters differs from bulk material melting and NP melting. Bulk melting is described by a sharp increase in atomic mobility of all atoms²⁹ and a steep rise in a caloric curve (a graph of cluster energy vs. temperature) at the melting point, indicating a first-order phase transition. NP melting, on the other hand, is often characterized by surface melting followed by melting of the NP core^{8,30}. For nanoclusters, the process of "melting" involves a dynamic coexistence between ordered and disordered phases, a phenomenon generally not seen in nanoparticles or bulk materials^{31–33}.

Because NP and nanocluster melting generally occurs on length scales and time scales that are difficult to resolve experimentally, molecular simulation is often employed. Monte Carlo (MC) methods can efficiently sample configurational potential energy surfaces and construct caloric curves to describe cluster phase transitions^{34–36}. Molecular dynamics (MD) simulations construct time trajectories of atoms by directly integrating Newton's equations of motion. Forces between atoms are calculated with an interatomic potential ($F = -\nabla E$). Classical molecular dynamics uses models of the interatomic potential with parameters fit to some combination of experimental data and quantum mechanical calculations, such as density functional theory (DFT).

It is possible to use DFT to compute interatomic potentials at each time step in an MD simulation – sometimes referred to as Born-Oppenheimer MD (BOMD) or *ab initio* MD³⁷. This method is more accurate but is considerably more computationally expensive (prohibitively expensive for clusters of tens of atoms). BOMD has been used to simulate the melting of palladium clusters³⁸ and gallium clusters with changing electronic properties or competing stable solid phases^{39–44}.

This study uses classical MD simulation because of its accessibility and computational feasibility. Moreover, classical MD lends itself more readily to subsequent

analyses involving more complex processes relevant to CNT growth (e.g., surface adsorption/desorption, diffusion, carbon dissolution, and formation of graphitic carbon). Magic numbers in Fe have been studied in small nanoclusters with both experiments⁴⁵ and spin polarization DFT simulations to capture magnetic properties^{25,46–49}. Although classical MD simulations do not capture detailed electronic magic number effects (e.g., Fe₇ and Fe₁₅), geometric magic numbers (e.g., Fe₁₃) and their properties can be extracted and may be relevant to other transition metal atoms apart from Fe.

The paper is organized as follows. Section II details the MD simulation method and the associated nanocluster structural and thermodynamic analysis. Section III summarizes the results of the calculations of Fe nanocluster melting and phase transition characteristics. Section IV discusses the relationship between nanocluster size and structure and its melting behavior. Finally, concluding remarks are summarized in Section V.

II. METHODS

Molecular dynamics (MD) simulations were used to investigate cluster melting. In MD, discrete atoms are simulated in a periodic box and their motion is integrated forward in time, abiding by Newton's equations of motion ($F = ma$).

Classical MD, which uses simple interatomic potentials, can access larger lengthscales and timescales than quantum mechanical methods. However, some long-time- and length-scale phenomena (e.g., vapor condensation, leading to nucleation and growth of large numbers of NPs) are still prohibitively expensive because MD must account for every atom's movement. Despite these limitations, MD is still useful for gaining insights into atomic-scale phenomena that cannot be experimentally observed, such as the individual nanocluster phase transitions analyzed in this work.

Cluster melting data was obtained with classical MD simulations using the open-source LAMMPS (Large Atomic/Molecular Massively Parallel Simulator) software⁵⁰ with an embedded atom method Finnis-Sinclair (EAM-FS)⁵¹ many-body interatomic potential for Fe. The potential energy of a given atom i is given by

$$E_i = F_\alpha \left(\sum_{j \neq i} \rho_{\alpha\beta}(r_{ij}) \right) + \frac{1}{2} \sum_{j \neq i} \phi_{\alpha\beta}(r_{ij}), \quad (2)$$

where F_α is the embedding energy, a function of the (modeled) electron density, $\rho_{\alpha\beta}$, contributed by neighboring atom j of element β at the site of atom i of element α . $\phi_{\alpha\beta}$ is a simple pair potential between atoms i and j . The potential was parameterized to reproduce solid and liquid characteristics of Fe⁵². Solid state

binding energies agreed with those calculated using density functional theory (DFT) (supplementary material Fig.S1-3). Furthermore, the boiling point and latent heat of vaporization were validated using MD simulations of direct vapor-liquid co-existence (supplementary material Fig.S4).

Global minimum energy configurations for Fe_n clusters for up to 100 atoms from Elliot et al.⁵³ (obtained with basin-hopping energy minimization) were used as starting configurations for Fe cluster structure optimization. The EAM-FS potential used in this work had a different parametrization than the that used in Ref.⁵³. New minimum energy configurations for most of the cluster sizes were obtained using parallel tempering (PT) MD simulations, also called replica-exchange MD (*fix temper* in LAMMPS). In the PT simulations, 90 replicas of individual Fe_n clusters were run concurrently in the canonical ensemble (NVT – constant number of atoms, N ; volume, V ; and temperature T) at 90 different temperatures from 250 K to 2500 K in increments of 25 K. Simulations were initiated at the global minimum energy configurations for 21 ns (1 ns warm-up time and 20 ns where data was collected) with a 1 fs timestep. Every 100 timesteps, each replica is proposed to swap with the replica at the temperature above it with a Metropolis acceptance probability:

$$P^{acc} = \min \left[1, \exp \left(\left(\frac{1}{k_B T_1} - \frac{1}{k_B T_2} \right) (E_1 - E_2) \right) \right], \quad (3)$$

where k_B is Boltzmann's constant, and T_i and E_i are the temperatures and energies of the lower (1) and next higher (2) temperature replica, respectively. The exchanges between replicas allow for good sampling of configurations that lie on opposing sides of an energy barrier, as each replica is able to achieve high temperatures to overcome these barriers. The replica trajectories (which traversed a wide range of temperatures) were reordered into isothermal trajectories at the 90 chosen temperatures. The lowest temperature trajectory should be a good sampling of the low-energy configurations of any given cluster size. For more than 2/3 of the cluster sizes, new lower energy configurations were obtained (after energy minimization with the LAMMPS *minimize* command) from these low-temperature trajectories.

At lower temperatures and larger cluster sizes, as well as at temperatures of large first-order-like phase transitions, P^{acc} for certain replicas can decrease to values that preclude adequate traversal between temperatures. Excluding lower temperatures (if possible), decreasing the spacing between adjacent temperatures, or employing longer simulation times can compensate for this effect. PT simulations were used in part to obtain correct low-energy configurations for subsequent calculations and observations and in part to adequately sample cluster thermodynamic space to calculate caloric curves, heat capacities, and melting temperatures. Thermodynamic data for these calculations were collected every 10

timesteps, including kinetic and potential energy. Heat capacity was calculated from the fluctuations in potential energy:

$$\frac{C_v}{k_B} = \frac{\langle E_{pot}^2 \rangle - \langle E_{pot} \rangle^2}{nk_B^2 T^2} + \frac{3}{2}, \quad (4)$$

where $\langle E_{pot} \rangle$ is the average potential energy of the cluster over the simulation time, T is temperature. The 3/2 term is added as a kinetic contribution. Melting points, T_{C_v} , were defined as the temperature of maximum C_v for clusters with first-order-like phase transitions, and the temperature of largest C_v slope for clusters with second-order-like phase transitions.

Simple single-cluster isothermal MD simulations were also run for further mechanistic melting analysis. The simulations were initiated from the global minimum energy configurations obtained from the PT simulations and run in the NVT ensemble for 20 ns at 75 temperatures from 50 K to 3750 K in increments of 50 K, with atomic configurations collected every 1 ps. For all PT and simple NVT simulations in this work, the canonical stochastic Langevin dynamics thermostat⁵⁴ (*fix temp/cslid* in LAMMPS) was invoked every 100 timesteps. Atomic Lindemann indices:

$$\delta_i = \frac{1}{n-1} \sum_{i \neq j} \frac{\sqrt{\langle r_{ij}^2 \rangle - \langle r_{ij} \rangle^2}}{\langle r_{ij} \rangle}, \quad (5)$$

and whole cluster Lindemann index:

$$\delta_c = \frac{2}{n(n-1)} \sum_{i > j} \frac{\sqrt{\langle r_{ij}^2 \rangle - \langle r_{ij} \rangle^2}}{\langle r_{ij} \rangle}, \quad (6)$$

were calculated at each temperature to measure increases in atomic motion due to melting. A time average is represented by $\langle \rangle$ and r_{ij} is the pairwise distance between atoms of indices i and j . The atomic distance from the cluster center of mass (CoM), $r_{i,CoM}$, was also calculated for each temperature to yield structural information about core melting.

III. RESULTS

Molecular dynamics simulations were performed for individual clusters with up to 100 atoms at temperatures spanning the melting transition. Three types of clusters are useful to delineate (Fig.1) and will be used throughout this work: 1) **Closed-shell clusters** are clusters with symmetric, closed-shell global minimum energy structures. 2) **Near-closed-shell clusters** are 1 to a few atoms away from closed-shell structures. Both closed-shell- and near-closed-shell clusters are considered *magic number clusters*. 3) **Far-from-closed-shell clusters** are distant in size to highly symmetric minimum-energy structures. These are considered *non-magic number clusters*.

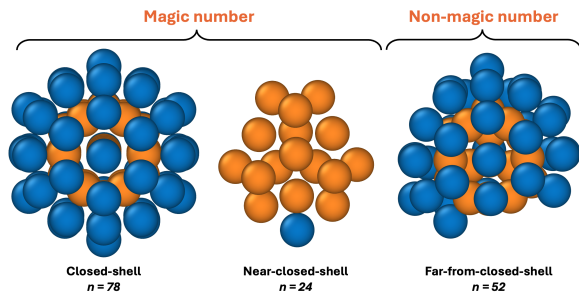


Figure 1. Snapshots of Fe nanoclusters of 3 types. Core (orange) and shell (blue) atoms are colored for clarity. Fe_{78} (left) is a closed-shell cluster composed of two interpenetrating double-shelled icosahedrons. Fe_{24} (middle) is a near-closed-shell cluster, with one extra atom attached to 3 interpenetrating single-shelled icosahedrons. Fe_{52} (right) is a far-from-closed-shell cluster with an icosahedral core, but many atoms are missing from its second shell. Both Fe_{78} and Fe_{24} are considered *magic number* clusters, while Fe_{52} is considered a *non-magic number* cluster.

Closed-shell (magic number) sizes have deeper global minima energy configurations than far-from-closed-shell nanoclusters. For this reason, the range of temperatures over which a cluster melts (escapes the global minimum potential energy well) can vary strongly. Moreover, due to the presence of many configurations that are close in energy and the dynamic-coexistence (isomerization) nature of nanocluster melting³¹⁻³³, a single unambiguous melting point temperature can be difficult to identify. This work attempts to demystify Fe cluster melting by analyzing cluster energetics and mechanisms of melting with cluster structure in mind.

A. Cluster energetics

To quantify the melting behavior of iron clusters, caloric curves of total energy (eV/atom) vs. temperature (K) were obtained for each cluster size. Each data point corresponds to a stitched-together (reordered) parallel tempering MD trajectory at one cluster size and temperature (Fig.2). Temperature was determined from time-averaged cluster kinetic energies ($T_{MD} = 2 \frac{E_{kin}}{k_B}$), corrected for whole-cluster translational degrees of freedom absent in the single-cluster MD simulations: $T = \frac{T_{MD}}{3n-3}$.

Caloric curves qualitatively differ by cluster size – a phenomenon that this work attempts to address. *Closed-shell* magic number clusters (Fe_{13} and Fe_{19} and more not shown – many have perfect or interpenetrating icosahedral structures) exhibit phase transitions with large increases in total energy upon melting relative to neighboring clusters. This phenomenon can be seen in the large vertical spaces between the curves in the solid region (left) of Fig.2.

In general, specific energy decreases with cluster size, n : $E_{n-1} > E_n > E_{n+1}$. A cluster with a higher n

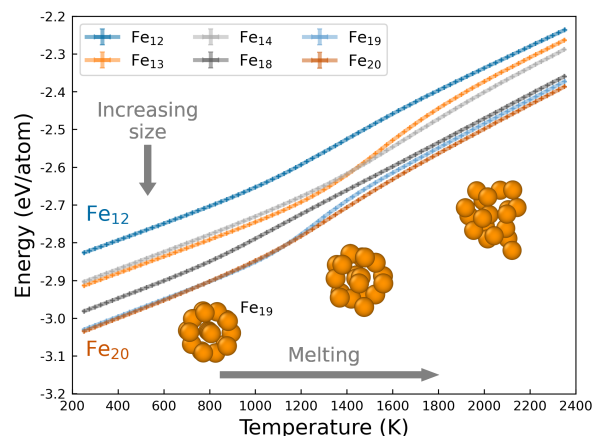


Figure 2. MD caloric curves for selected clusters from Fe_{12} - Fe_{20} . Each point corresponds to an isothermal trajectory from parallel tempering simulations. The closed-shell clusters (Fe_{13} in orange and Fe_{19} in light blue) have larger spacings in energy than their neighboring sizes in the solid (left) region.

has more bonds per atom due to a smaller surface-to-volume ratio, leading to a lower specific energy. Accordingly, the *difference* in specific energy between adjacent sizes (spacing between curves) generally decreases with increasing n , as the difference in surface-to-volume ratios decreases with greater n . The trend is violated in the solid phase regime (left) for closed-shell magic number clusters, whose energy curves then cross their $n+1$ neighbor cluster (Fe_{14} and Fe_{20} in Fig.2) upon phase transition into the liquid phase regime (right), restoring the trend.

Heat capacity curves were calculated from the PT simulations for each cluster size to aid in melting point determination and cluster melting classification. Individual C_v curves normalized by k_B and n are given for closed-shell cluster Fe_{13} , near-closed-shell cluster Fe_{77} , and far-from-closed-shell Fe_{51} in Fig.3a-c. These C_v curves qualitatively vary more starkly than the caloric curves, and this work attempts to investigate these differences. Most cluster sizes have notable peaks in C_v corresponding to the latent heat present in first-order-like phase transitions. Within the size range studied, larger clusters tended to have sharper C_v peaks at lower temperatures than smaller clusters. Closed-shell and most near-closed-shell clusters – including both Fe_{13} and Fe_{77} in Fig.3a-b – exhibit such first-order-like phase-transition peaks in their C_v curves. The energetic melting temperature, T_{C_v} , is defined as the temperature of maximum heat capacity in these clusters. This maximum heat capacity, $\max(C_v)$, can be thought of as a proxy for the latent heat of melting for the cluster, which will be discussed later on.

Almost 30 cluster sizes in the range studied do not show any pronounced peak in C_v (e.g., Fe_{51} in Fig.3c), having either a very small or non-existent latent heat of melting and indicating a second-order-like phase tran-

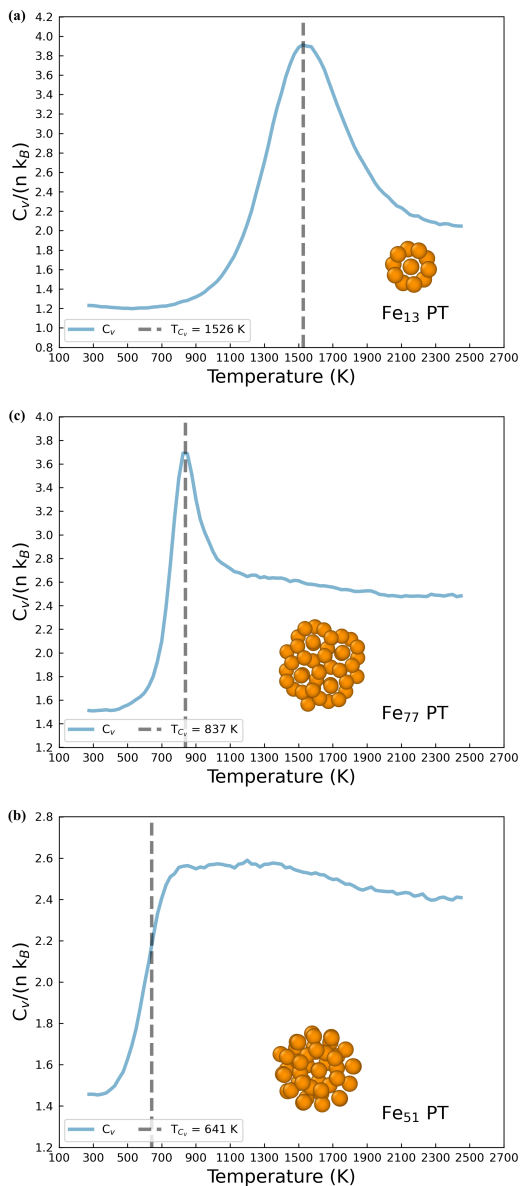


Figure 3. Heat capacity curves for 3 selected cluster sizes: (a) Closed-shell Fe_{13} has a first-order-like phase transition with a tall and wide peak at a high melting point. (b) Near-closed Fe_{77} also has a first-order-like transition but with a narrower peak and a lower melting point due to its larger size. (c) Far-from-closed Fe_{51} has a second-order-like phase transition with no pronounced peak in its heat capacity curve.

sition. For these clusters, the T_{C_v} was defined as the temperature of maximum gradient (steepest ascent) in C_v . Heat capacity curves for all cluster sizes from 10-100 atoms can be found in the SI.

At the temperatures near a phase transition region in a PT simulation with uniform temperature spacing, the acceptance probability, P^{acc} , of parallel tempering replica swaps is decreased due to less overlap of energies between adjacent replicas. Acceptance ratios for the PT simulations outlined in section II are given in Fig.4a-c

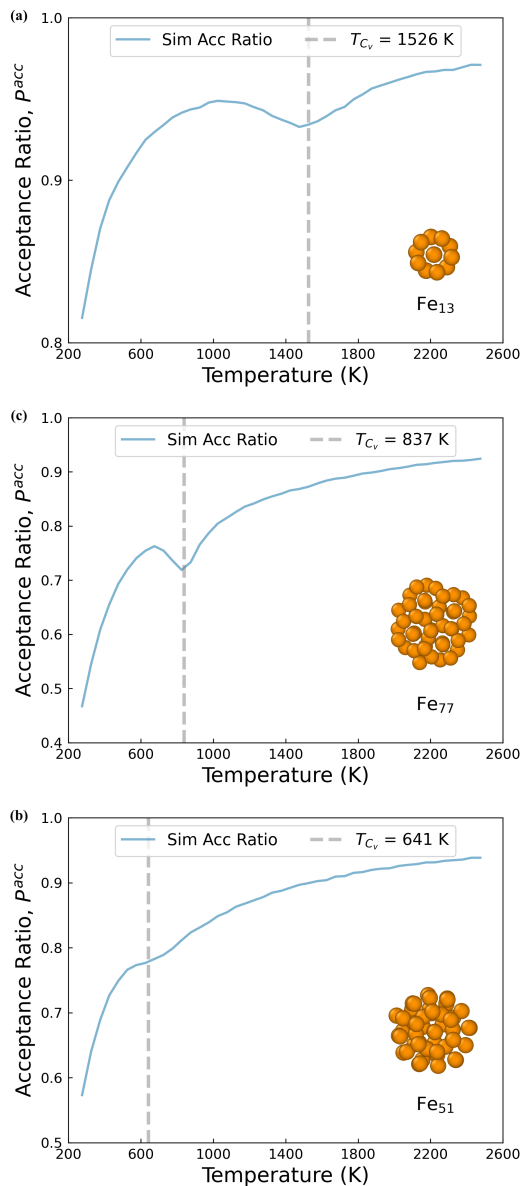


Figure 4. Acceptance ratio curves during parallel tempering MD simulations of (a) closed-shell Fe_{13} and (b) near-closed Fe_{77} – which both show large P^{acc} dips at their phase transition temperatures – and (c) far-from-closed Fe_{51} which features a dent in its P^{acc} at T_{C_v} defined from its heat capacity curve.

for Fe_{13} , Fe_{77} , and Fe_{51} .

In cluster sizes exhibiting first-order-like phase transitions, P_{acc} shows notable dips at T_{C_v} especially at lower temperatures. For far-from-closed-shell cluster sizes exhibiting second-order-type phase transitions, the dip in P_{acc} turns into a “dent”. The dent in P_{acc} for Fe_{51} at 500-800 K deviates from the temperature of $\max(C_v)$, which would lie around 1200 K. Even if the temperature of $\max(C_v)$ lay at the top of the step-edge in Fig.3c around 900 K, this is still above the temperature range of the dent in P_{acc} . Acceptance ratio plots for all cluster

sizes examined can be found in the SI.

To show how the C_v curves evolve across cluster sizes, several adjacent C_v curves are plotted in series for different size ranges in Figs. 5a-c. While adjacent C_v curves can differ from each other at low temperatures, curves for adjacent sizes converge at higher temperatures once all clusters are completely melted with no memory of their solid-state configurations. The temperature of convergence upon melting is largest for smaller clusters (near 1600 K in Fig. 5a), and decreases at larger cluster sizes to around 1400 K in Fig. 5b and 1250 K in Fig. 5c. From sizes 10-30, new stable closed shells can be attained with smaller differences in cluster size. Clusters with 13, 19, 23, and 26 atoms are all closed-shell sizes, so most small clusters are near-closed-shell and first-order-like in melting transition, with Fe_{30} as the first second-order-like melter (Fig. 5a). Clusters between 30 and 50 atoms mostly melt in a second-order-like fashion, except for a few clusters with varying strengths of first-order-like peaks, sometimes at very low temperatures for Fe_{34} and Fe_{40} (Fig. 5b). This “wing” peak motif in C_v is noted in Frantz et al. in LJ Ar³⁵. At large cluster sizes, closed-shell clusters are generally sparse, with many clusters before and after having smaller first-order-like C_v peaks at similar temperatures (Fig. 5c).

Even for clusters with pronounced first-order-like C_v peaks (e.g. clusters Fe_{78} through Fe_{85} in Fig. 5c), one can see an underlying step function-like curve with a discontinuity underneath the phase-transition peak. Many cluster heat capacity curves appear as a combination of first- and second-order-like phase transitions, where different sizes have first-order-like peaks ranging from large to small to absent, corresponding to a second-order-like transition (e.g. Fe_{86} in Fig. 5c).

As mentioned, the $\max(C_v)$ can be a proxy for the latent heat of melting for the cluster. In an ideal case, one would integrate the C_v over the cluster’s melting range to obtain the value of the latent heat; however, it is impossible to systematically identify a cluster’s melting range, as C_v before and after melting are generally not constants. It is also likely that the melting ranges of different cluster sizes vary strongly, making $\max(C_v)$ only a qualitative indicator of a cluster’s latent heat of melting. Nonetheless, a low $\max(C_v)$ could be a litmus test for clusters with second-order-like phase transitions.

The evolution of the strength of the first-order peaks can also be monitored with $\max(C_v)$, as symmetric closed-shell clusters have higher peaks than their neighboring sizes, which have higher maxima than far-from-closed-shell clusters with potentially second-order melting. Fig. 6 compares T_{C_v} and $\max(C_v)$ as a function of cluster size, with closed-shell cluster size (orange points) and sizes with second-order-like transitions (blue points) indicated.

A high maximum in C_v (i.e. proximity to a closed-shell structure) has a relatively weak effect on T_{C_v} ; many smaller closed-shell sizes having lower melting points than the few cluster sizes that follow (e.g., T_{C_v} for Fe_{14} - Fe_{17} are higher than that of Fe_{13}). The broad

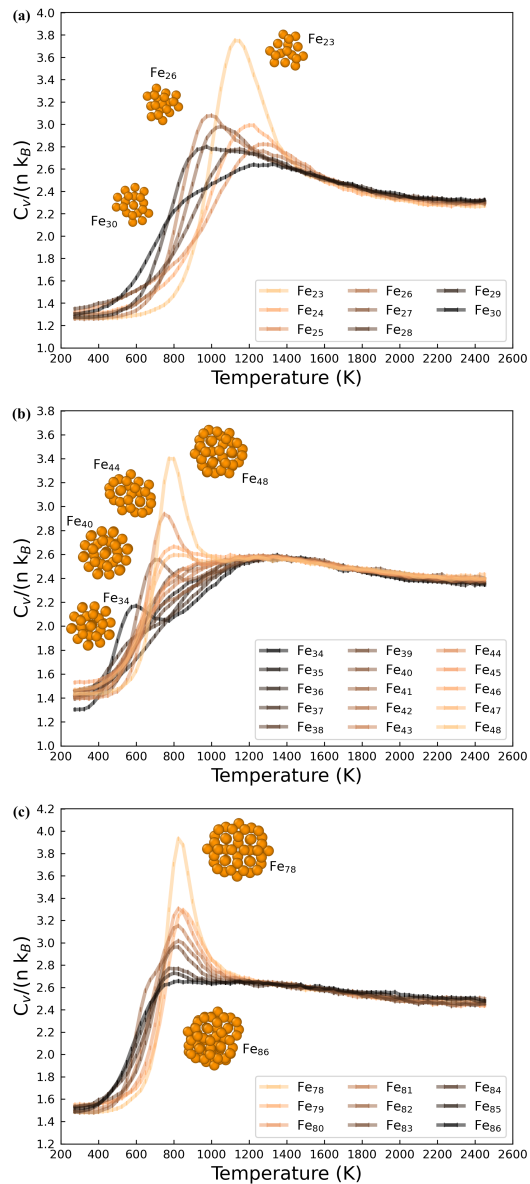


Figure 5. Selected series of consecutive C_v curves including clusters with first- and second-order-like phase transitions for (a) Fe_{23} - Fe_{30} (structure snapshots for closed-shell Fe_{23} , Fe_{26} and far-from-closed Fe_{30}), (b) Fe_{33} - Fe_{48} (structure snapshots for closed-shell Fe_{48} and Fe_{44}), and (c) Fe_{78} - Fe_{86} (structure snapshots for closed-shell Fe_{78} and far-from-closed Fe_{86}).

“horns” in $\max(C_v)$ in Fig. 6 from Fe_{53} to Fe_{69} , Fe_{75} to Fe_{85} , and Fe_{88} to Fe_{93} seem to confer higher melting points than the second-order-like melting sizes around them (though, the definition of the second-order transitions yield lower T_{C_v} regardless). Among adjacent clusters within the horns in $\max(C_v)$, clusters tend to build upon a basic structure (e.g., the 3 interpenetrating icosahedra in the bottom structure of Fe_{60}) until a transition to a more accommodating structure is available (like the stacked 4 interpenetrating icosahedra in the left structure of Fe_{78} - this structure first appears

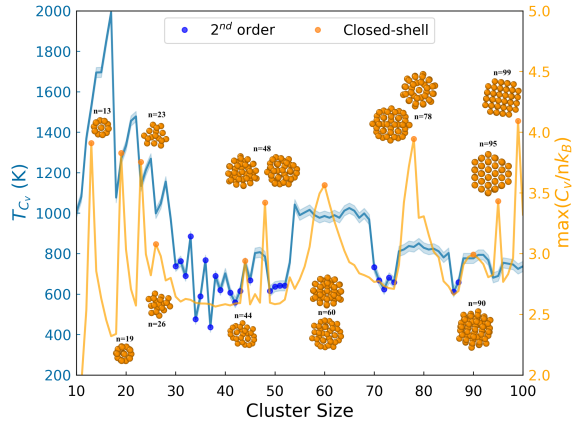


Figure 6. Dual plot of T_{C_v} and $\max(C_v/nk_B)$ as a function of cluster size. Closed-shell cluster structures are shown.

in Fe_{75} at the beginning of the $\max(C_v)$ horn). Elevated T_{C_v} is observed for clusters across the $\max(C_v)$ horns, potentially due to stable core structures conserved across each horn. The isolated bcc lattice clusters favored in Fe_{95} and Fe_{99} signify the beginning of the size range where bulk Fe structures become preferable to icosahedral-dominant geometries present in the rest of the cluster sizes.

B. Atomic mobility within clusters

Further investigating the cluster phase transitions, the Lindemann index²⁹ (δ_c) was calculated from each NVT MD trajectory. δ_c is often used to quantify the melting of clusters because it measures changes in atomic mobility in a solid, rapidly increasing upon initiation of atom movement. The temperature at which δ_c increases sharply is defined as the cluster's surface melting temperature, T_{δ_c} .

Plots of the Lindemann index vs. temperature for closed-shell Fe_{44} , near-closed Fe_{43} , and far-from-closed-shell Fe_{51} are given in Figs.7a-c. For these 3 (and most other) clusters, T_{δ_c} captures the early stages of melting and is much lower than T_{C_v} .

For clusters smaller than 50 atoms, closed-shell clusters have much higher T_{δ_c} than their near neighbors (e.g., the surface of Fe_{19} melts at 900 K, whereas Fe_{20} 's surface melts at 350 K – see Fig.10). While the trend continues through closed-shell Fe_{48} and its neighbors, larger near-closed-shell clusters do not have significantly lower T_{δ_c} than their corresponding closed-shell sizes. The δ_c vs. temperature plots for all cluster sizes studied can be found in the SI.

The phenomenon for small clusters can be observed on the scatterplot of T_{C_v} and T_{δ_c} in Fig.8. Surface melting of clusters 1, 2, or 3 atoms away from closed-shell structures is several 100s of K lower than closed-shell surface melting.

For more detailed mechanistic information on atom

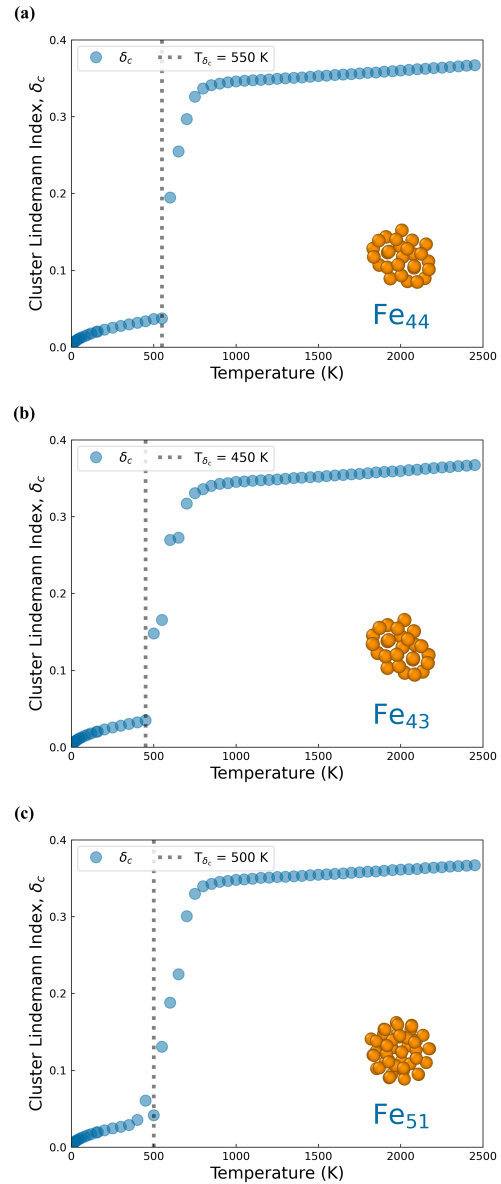


Figure 7. Plots of whole-cluster Lindemann index, δ_c , for (a) closed-shell Fe_{44} , (b) near-closed Fe_{43} , and (c) far-from-closed Fe_{51} throughout melting. Temperatures of surface melting, T_{δ_c} , are denoted by vertical dotted gray lines. While both Fe_{44} and Fe_{43} have low surface melting temperatures, the surface of Fe_{43} melts first.

position and mobility during melting, atomic Lindeman indices, δ_i , and atomic distance from cluster center-of-mass (CoM), $r_{i,CoM}$, were calculated from the NVT simulation trajectories at each temperature. 2D projection plots of δ_i , $r_{i,CoM}$, and temperature are shown for 2 pairs of closed-shell and near-closed-shell clusters in Figs.9a-d: sizes 13 and 14, and 78 and 77. In the left plots for Figs.9a-d, δ_i is plotted as a function of temperature and colored by the atoms distance from the cluster CoM (purple is closer to the center, yellow is closer to the surface). In the middle plots, $r_{i,CoM}$ is

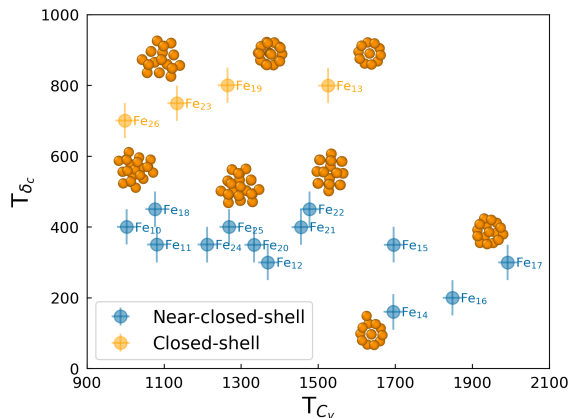


Figure 8. Scatter plot of T_{C_v} and T_{δ_c} for small cluster sizes. Near-closed shell clusters (blue) have lower surface melting temperatures T_{δ_c} than closed-shell clusters (orange).

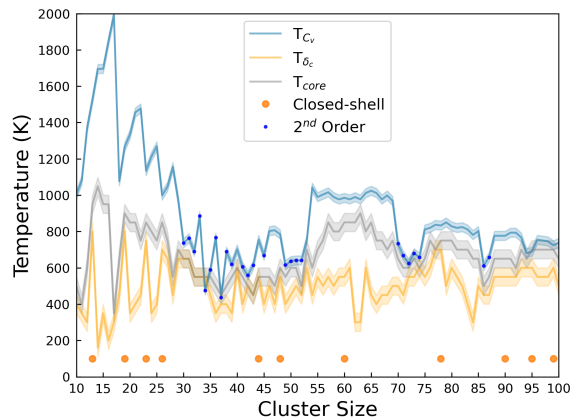


Figure 10. Plot of melting temperatures T_{C_v} (blue), T_{δ_c} (orange), and T_{core} (gray), as a function of cluster size. Closed-shell clusters are indicated with orange points, and sizes with second-order-like phase transitions are shown with dark blue dots on the T_{C_v} curve.

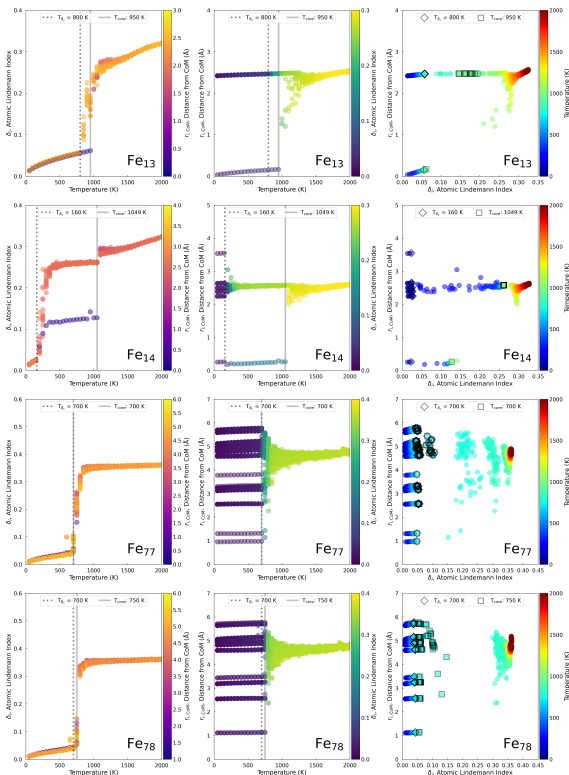


Figure 9. 2D projection plots of atomic Lindemann indices, δ_i , atomic distance from cluster CoM, $r_{i,CoM}$, and temperature for closed-shell Fe_{13} and Fe_{78} , and near-closed Fe_{14} and Fe_{77} . Two variables are plotted with the third variable incorporated into the color map. Surface melting, T_{C_v} , and core melting, T_{core} , are indicated on each plot.

plotted as a function of temperature and colored by δ_i (purple is more static, and green is more mobile). In the right plots, $r_{i,CoM}$ is a function of δ_i , colored by temperature (blue is cold and red is hot).

The use of $r_{i,CoM}$ allows us to visualize the shells of cluster atoms and measure core melting (interlayer

mixing). Using this value, the core melting temperature, T_{core} , was defined as the temperature at which the closest atom to the center of mass begins to mobilize. For both Fe_{13} and Fe_{14} (Figs.9a-b), the cluster cores (inner atom) mobilize at much higher temperatures than the surface atoms. Because Fe_{14} is small and near-closed, it mobilizes its extra atom at the surface at an extremely low temperature of 160 K, but its core remains unmoved until 1049 K, a higher temperature than it takes to melt both the surface and core of Fe_{13} ! The larger sizes Fe_{77} and Fe_{78} (Figs.9c-d), however, do not behave the same way, with their surfaces and cores melting around the same temperature of 700-750 K. The 2D projection plots for all cluster sizes examined are available in the SI.

While not present in Fe_{77} and Fe_{78} , premelting (shell-before-core melting) was commonly observed for larger clusters in differences between T_{δ_c} , and T_{core} of 100 K to several 100s of K. All melting points (T_{C_v} , T_{δ_c} , and T_{core}) are plotted as a function of cluster size in Fig.10. Small clusters under 30 atoms, and sizes in the T_{C_v} “shelves” between 53 and 69, and between 75 and 85, exhibit large spaces between all 3 melting temperatures (except for the high T_{δ_c} ’s for closed-shell sizes 13, 19, 23, 26, and 78). There is also a light correlation between T_{core} and T_{C_v} for these size ranges. The closed-shell sizes 44, 48, 60, 90, 95, and 99 have no clear special influence on T_{δ_c} or T_{core} . Most closed-shell sizes (except 44 and 95) have elevated T_{C_v} , and confer elevated T_{C_v} to neighboring near-closed-shell sizes.

IV. DISCUSSION

As mentioned above, the solid-liquid phase transition in small Fe nanoclusters differs from melting in bulk Fe and even Fe nanoparticle melting. This anal-

ysis suggests that nanocluster melting for sizes under 30 atoms differs from cluster melting above 30 atoms. And the melting of nanoclusters from 30-50 atoms differs from cluster melting above 50 atoms! Finally, given the appearance of stable bcc chunks of Fe in the 90-atom range, the melting of these nanoclusters and larger likely compose a regime of their own, blending into nanoparticle behavior and Gibbs-Thompson melting point depression.

A. Below 30 atoms

For nanoclusters under 30 atoms, melting begins with surface atoms swapping places with each other ($T_{\delta_c} < T < T_{core}, T_{C_v}$). Eventually, the cluster’s central atom(s) breaks free ($T_{core} < T < T_{C_v}$), and the cluster forms different structures with higher potential energies (liquid) and short lifetimes. At higher temperatures, the higher potential energy structures become longer-lived ($T > T_{C_v}$), eventually pushing the cluster into the disordered liquid state.

Considering the classes of closed-shell and near-closed-shell clusters, there are large differences in T_{δ_c} and T_{core} , which represent the beginning of “atom-swapping” and intralayer mixing to form higher potential energy configurations, respectively. Near-closed-shell and closed-shell clusters maintain similar core melting temperatures (T_{core}). However, near-closed-shell clusters, especially those with 1 extra atom relative to a closed-shell have drastically lower T_{δ_c} compared to their closed-shelled neighbors. Low-temperature surface melting of near-closed-shell cluster size surface melting at low temperatures has been observed in simulations of Al clusters²¹. Early surface melting might make sense to delocalize extra atoms or holes with many dangling bonds through atomic movement at low temperatures.

Cluster energetics are impacted by these shell closings as well. While T_{C_v} is elevated for closed-shell clusters, the melting point is even higher for near-closed-shell clusters with 1-3 more atoms than the closed-shell. This may be attributed to the retained stability from the closed shell structure, plus the buffer of storing excess energy in the degrees of freedom of the extra atoms on the surface.

B. Between 30 and 50 atoms

At and above 30 atoms, melting becomes more complicated. The absence of pronounced heat capacity (C_v) peaks is common, with most cluster sizes between 30 and 50 atoms undergoing second-order-like phase transitions. Second-order phase transitions in clusters have been reported in cases where the system undergoes a semi-conducting to metallic transition or shift in magnetic moment^{55,56}, neither of which are modeled in the classical MD potential in this work. For this reason, the

second-order-like nature of the cluster phase transitions must come from geometric structural factors. Perhaps restructurings occur in these clusters that allow for entropic relaxation equal to or exceeding the energy requirement of mobilizing internal atoms.

It is also peculiar that the 2 closed-shell cluster sizes (Fe_{44} and Fe_{48}) were surrounded by near-closed-shell clusters with no pronounced first-order-like heat capacity peak. Upon analyzing the structures of the global minimum configurations of these clusters, shifts in cluster symmetry did not explain these qualitative differences in C_v .

C. Above 50 atoms

Melting above 50 atoms is described by similarity to nanoparticle melting, with premelting (surface melting) manifesting in a large difference between T_{δ_c} and T_{core} . Premelting is especially stark in size regions of long “shelves” of elevated T_{C_v} and T_{core} . These shelves likely exist because clusters have a stable closed-shell core, with island structures accumulating on the surface until a new core (and a new shelf of high T_{C_v} and T_{core}) is formed. Between the shelves of high T_{C_v} are far-from-closed-shell clusters with small $\max(C_v)$ and second-order-like melting behavior.

Near-closed-shell sizes no longer have premature surface melting (T_{δ_c}) compared to their closed-shell size, as observed for smaller cluster sizes. This may be explained by the ability of large clusters to better accommodate extra atoms or holes by contorting certain parts of the larger structure. In this case, there would not be as much energy gained by the low-temperature delocalization of imperfections on the surface, which would be favorable for smaller cluster sizes.

D. Above 90 atoms

Melting in clusters with over 90 atoms appears less erratic than smaller cluster melting, with less variation in T_{C_v} , T_{δ_c} , and T_{core} . All cluster sizes seem to have first-order-like phase transitions, with bcc-structured clusters becoming energetically favorable over the radial icosahedral-dominant structures favored at smaller sizes. The presence of these bcc clusters indicates a transition into larger nanoparticle melting point scaling (Gibbs-Thompson) outlined in the Introduction.

V. CONCLUSION

Classical molecular dynamics simulations were used to investigate the melting of Fe nanoclusters up to 100 atoms (1.2 nm) in size. Strong cluster-to-cluster variations (magic number effects) were observed. Size-dependent melting behavior may confer size-dependent

disorder in real catalytic nanocluster systems at temperatures where some clusters are melted and others are not. Melted clusters with more disorder may have different catalytic activity from solid ones (or ones with a molten surface but a solid core). Differences in surface and core mixing can influence carbon adsorption, diffusion, and dissolution in CNT growth, leading to different growth rates or modes of CNT growth (tangential vs. perpendicular growth⁷).

Melting points T_{C_v} , T_{δ_c} , and T_{core} can affect the catalytic activity of Fe nanoclusters. In CNT growth, the mobilization of Fe surface atoms (T_{δ_c}) could accelerate the diffusion of C atoms on the NP surface, increasing the CNT growth rate. Mobilization of bulk atoms (T_{core}), however, could increase the solubility of carbon in Fe, requiring more C to be fed to the NPs and thus slowing the CNT growth rate. An increase in potential energy (T_{C_v}) associated with longer lifetimes of disordered isomers – with a disordered outer layer – may change both the adsorption energies and transport properties.

The key takeaways from this work are the following:

- The addition of one to two atoms in a cluster can cause strong variations in surface and core melting temperature and energetics. There may be implications for enhanced or suppressed catalytic activity through changes in species adsorption or transport on the cluster surface.
- Near-closed-shell clusters under 30 atoms have very high energetic melting points (T_{C_v}) – higher than the nearest closed-shell clusters, and very low surface melting points (T_{δ_c}).
- Many far-from-closed-shell clusters (and a few near-closed-shell clusters under 50 atoms) exhibited second-order-like phase transitions with no pronounced peak in C_v . Second-order phase transitions in clusters have only been reported in systems with concurrent transitions in electronic or magnetic behavior^{39,55} not modeled in the classical interatomic potential used in this work.
- Clusters larger than 50 atoms exhibited shelves of high T_{C_v} and T_{core} near and including closed-shells. Far-from-closed-shell clusters with second-order-like melting transitions separated the shelves from each other.
- BCC Fe clusters were favored at cluster sizes in the 90s of atoms, indicating a trend towards Gibbs-Thompson nanoparticle melting point scaling.
- Geometric magic number effects alone conferred a deviation from the Gibbs-Thomson melting point depression scaling followed by nanoparticles.

SUPPLEMENTARY MATERIALS

Additional materials such as data used in method benchmarking can be found in **SI.pdf**. Heat capacity curves, parallel tempering acceptance ratio plots, Lindemann index curves, atomic Lindemann index vs. distance from CoM plots for all cluster sizes, and snapshots of minimum energy configurations for many cluster sizes can be found in the **Cv-plots**, **Pacc-plots**, **lind-plots**, **delta-r-plots**, and **cluster-snapshots** folders, respectively.

ACKNOWLEDGMENTS

The support of Princeton University’s Andlinger Center for Energy and the Environment, and the Program in Plasma Science and Technology at the Princeton Plasma Physics Laboratory is gratefully acknowledged. In addition, this research utilized computing resources on the Princeton University Della and Stellar clusters.

COI statement: The authors have no conflicts of interest to disclose.

Data availability statement: The data are contained within the article and supplementary material.

Author contribution statement:

Louis E. S. Hoffenberg: conceptualization (equal); formal analysis (lead); writing – original draft preparation (lead). **Alexander Khrabry:** conceptualization (equal); formal analysis (supporting); review and editing (equal). **Yuri Barsukov:** conceptualization (equal); review and editing (equal). **Igor D. Kaganovich:** funding acquisition (supporting); conceptualization (equal); supervision (equal). **David B. Graves:** funding acquisition (lead); conceptualization (equal); review and editing (equal); supervision (equal).

REFERENCES

- ¹F. Tao, *Metal Nanoparticles for Catalysis: Advances and Applications* (Royal Society of Chemistry, 2014).
- ²T. Imaoka, H. Kitazawa, W.-J. Chun, S. Omura, K. Albrecht, and K. Yamamoto, “Magic Number Pt13 and Misshapen Pt12 Clusters: Which One is the Better Catalyst?” *Journal of the American Chemical Society* **135**, 13089–13095 (2013), publisher: American Chemical Society.
- ³A. Pescaglini and D. Iacopino, “Metal nanoparticle–semiconductor nanowire hybrid nanostructures for plasmon-enhanced optoelectronics and sensing,” *Journal of Materials Chemistry C* **3**, 11785–11800 (2015), publisher: Royal Society of Chemistry.
- ⁴K. McNamara and S. A. M. Tofail, “Nanoparticles in biomedical applications,” *Advances in Physics: X* **2**, 54–88 (2017).
- ⁵A. Puzetzyk, D. Geohagan, S. Jesse, I. Ivanov, and G. Eres, “In situ measurements and modeling of carbon nanotube ar-

- ray growth kinetics during chemical vapor deposition,” *Applied Physics A* **81**, 223–240 (2005).
- ⁶S. Helveg, C. López-Cartes, J. Sehested, P. L. Hansen, B. S. Clausen, J. R. Rostrup-Nielsen, F. Abild-Pedersen, and J. K. Nørskov, “Atomic-scale imaging of carbon nanofibre growth,” *Nature* **427**, 426–429 (2004), publisher: Nature Publishing Group.
- ⁷H. Amara and C. Bichara, “Modeling the Growth of Single-Wall Carbon Nanotubes,” *Topics in Current Chemistry* **375**, 55 (2017).
- ⁸K. K. Nanda, “Size-dependent melting of nanoparticles: Hundred years of thermodynamic model,” *Pramana* **72**, 617–628 (2009).
- ⁹T. L. Beck, J. Jellinek, and R. S. Berry, “Rare gas clusters: Solids, liquids, slush, and magic numbers,” *The Journal of Chemical Physics* **87**, 545–554 (1987), https://pubs.aip.org/aip/jcp/article-pdf/87/1/545/18964857/545_1_online.pdf.
- ¹⁰J. Jellinek, T. L. Beck, and R. S. Berry, “Solid–liquid phase changes in simulated isoenergetic Ar₁₃,” *The Journal of Chemical Physics* **84**, 2783–2794 (1986), https://pubs.aip.org/aip/jcp/article-pdf/84/5/2783/18957240/2783_1_online.pdf.
- ¹¹P. Pawlow, “Ober die Abhängigkeit des Schmelzpunktes von der Oberflächenenergie eines festen Körpers (Zusatz.),” *Zeitschrift für Physikalische Chemie* **65U**, 545–548 (1909), publisher: De Gruyter (O).
- ¹²C. Jackson and G. B. McKenna, “The melting behavior of organic materials confined in porous solids,” *The Journal of Chemical Physics* **93**, 9002–9011 (1990), publisher: American Institute of Physics.
- ¹³G. A. Breaux, R. C. Benirschke, T. Sugai, B. S. Kinnear, and M. F. Jarrold, “Hot and Solid Gallium Clusters: Too Small to Melt,” *Physical Review Letters* **91**, 215508 (2003), publisher: American Physical Society.
- ¹⁴M. Schmidt, R. Kusche, B. von Issendorff, and H. Haberland, “Irregular variations in the melting point of size-selected atomic clusters,” *Nature* **393**, 238–240 (1998), publisher: Nature Publishing Group.
- ¹⁵A. Susan, A. Kibey, V. Kaware, and K. Joshi, “Correlation between the variation in observed melting temperatures and structural motifs of the global minima of gallium clusters: An ab initio study,” *The Journal of Chemical Physics* **138**, 014303 (2013).
- ¹⁶K. Joshi, S. Krishnamurty, and D. G. Kanhere, ““Magic Melters” Have Geometrical Origin,” *Physical Review Letters* **96**, 135703 (2006), publisher: American Physical Society.
- ¹⁷S. L. Girshick, P. Agarwal, and D. G. Truhlar, “Homogeneous nucleation with magic numbers: Aluminum,” *The Journal of Chemical Physics* **131**, 134305 (2009).
- ¹⁸Z. H. Li, D. Bhatt, N. E. Schultz, J. I. Siepmann, and D. G. Truhlar, “Free Energies of Formation of Metal Clusters and Nanoparticles from Molecular Simulations: Al_n with n = 2–60,” *The Journal of Physical Chemistry C* **111**, 16227–16242 (2007).
- ¹⁹N. Gaston, “Cluster melting: new, limiting, and liminal phenomena,” *Advances in Physics: X* **3**, 1401487 (2018).
- ²⁰T. P. Martin, “Shells of atoms,” *Physics Reports* **273**, 199–241 (1996).
- ²¹A. Bagrets, R. Werner, F. Evers, G. Schneider, D. Schooss, and P. Wölfle, “Lowering of surface melting temperature in atomic clusters with a nearly closed shell structure,” *Physical Review B* **81**, 075435 (2010), publisher: American Physical Society.
- ²²A. Yalamanchali, K. L. Pyfer, and M. F. Jarrold, “Melting of Size-Selected Aluminum Clusters with 150–342 Atoms: The Transition to Thermodynamic Scaling,” *The Journal of Physical Chemistry C* **121**, 10242–10248 (2017), publisher: American Chemical Society.
- ²³E. C. Neyts and A. Bogaerts, “Numerical Study of the Size-Dependent Melting Mechanisms of Nickel Nanoclusters,” *The Journal of Physical Chemistry C* **113**, 2771–2776 (2009), publisher: American Chemical Society.
- ²⁴M. Sehrawat, M. Rani, S. Sharma, S. Bharadwaj, B. G. Falzon, and B. P. Singh, “Floating catalyst chemical vapour deposition (FCCVD) for direct spinning of CNT aerogel: A review,” *Carbon* **219**, 118747 (2024).
- ²⁵E. Kim, A. Mohrland, P. F. Weck, T. Pang, K. R. Czerwinski, and D. Tománek, “Magic numbers in small iron clusters: A first-principles study,” *Chemical Physics Letters* **613**, 59–63 (2014).
- ²⁶H. T. Diep, S. Sawada, and S. Sugano, “Melting and magnetic ordering in transition-metal microclusters,” *Physical Review B* **39**, 9252–9259 (1989), publisher: American Physical Society.
- ²⁷F. Ding, A. Rosén, and K. Bolton, “Size dependence of the coalescence and melting of iron clusters: A molecular-dynamics study,” *Physical Review B* **70**, 075416 (2004), publisher: American Physical Society.
- ²⁸A. Khrabry, L. E. S. Hoffenberg, I. D. Kaganovich, Y. Barsukov, and D. B. Graves, “Gibbs free energies of Fe clusters can be approximated by Tolman correction to accurately model cluster nucleation and growth,” (2024), arXiv:2408.16693 [cond-mat.mtrl-sci].
- ²⁹F. A. Lindemann, “The calculation of molecular Eigenfrequencies,” Tech. Rep. (1984).
- ³⁰R. Huang, Y.-H. Wen, Z.-Z. Zhu, and S.-G. Sun, “Two-Stage Melting in Core–Shell Nanoparticles: An Atomic-Scale Perspective,” *The Journal of Physical Chemistry C* **116**, 11837–11841 (2012), publisher: American Chemical Society.
- ³¹S. A. Rice, *Evolution of Size Effects in Chemical Dynamics, Volume 70, Part 2* (John Wiley & Sons, 2009).
- ³²D. Schebarchov and S. C. Hendy, “Solid-liquid phase coexistence and structural transitions in palladium clusters,” *Physical Review B* **73**, 121402 (2006), publisher: American Physical Society.
- ³³A. Aguado, “Neither solid nor liquid,” *Nature Materials* **15**, 931–933 (2016), publisher: Nature Publishing Group.
- ³⁴S. Srinivas and J. Jellinek, “Ab initio Monte Carlo Investigations of Small Lithium Clusters,” *physica status solidi (b)* **217**, 311–322 (2000).
- ³⁵D. D. Frantz, “Magic number behavior for heat capacities of medium-sized classical Lennard-Jones clusters,” *The Journal of Chemical Physics* **115**, 6136–6157 (2001).
- ³⁶E. Yurtsever and F. Calvo, “Many-body effects on the melting and dynamics of small clusters,” *Physical Review B* **62**, 9977–9980 (2000), publisher: American Physical Society.
- ³⁷R. Car and M. Parrinello, “Unified Approach for Molecular Dynamics and Density-Functional Theory,” *Physical Review Letters* **55**, 2471–2474 (1985), publisher: American Physical Society.
- ³⁸A. Luna-Valenzuela, J. N. Pedroza-Montero, A. M. Köster, P. Calaminici, L. E. Gálvez-González, and A. Posada-Amarillas, “Pd₈ Cluster: Too Small to Melt? A BOMD Study,” *The Journal of Physical Chemistry A* **128**, 572–580 (2024), publisher: American Chemical Society.
- ³⁹D. C. Wallace, “Melting of elements,” *Proceedings of the Royal Society of London. Series A: Mathematical and Physical Sciences* **433**, 631–661 (1997), publisher: Royal Society.
- ⁴⁰G. A. Breaux, D. A. Hillman, C. M. Neal, R. C. Benirschke, and M. F. Jarrold, “Gallium Cluster “Magic Melters”,” *Journal of the American Chemical Society* **126**, 8628–8629 (2004), publisher: American Chemical Society.
- ⁴¹K. G. Steenbergen, D. Schebarchov, and N. Gaston, “Electronic effects on the melting of small gallium clusters,” *The Journal of Chemical Physics* **137**, 144307 (2012).
- ⁴²K. G. Steenbergen and N. Gaston, “Geometrically induced melting variation in gallium clusters from first principles,” *Physical Review B* **88**, 161402 (2013), publisher: American Physical Society.
- ⁴³K. G. Steenbergen and N. Gaston, “Quantum Size Effects in the Size–Temperature Phase Diagram of Gallium: Structural Characterization of Shape-Shifting Clusters,” *Chemistry – A European Journal* **21**, 2862–2869 (2015).

- ⁴⁴K. G. Steenbergen and N. Gaston, “Two worlds collide: Image analysis methods for quantifying structural variation in cluster molecular dynamics,” *The Journal of Chemical Physics* **140**, 064102 (2014).
- ⁴⁵M. Sakurai, K. Watanabe, K. Sumiyama, and K. Suzuki, “Magic numbers in transition metal (Fe, Ti, Zr, Nb, and Ta) clusters observed by time-of-flight mass spectrometry,” *The Journal of Chemical Physics* **111**, 235–238 (1999).
- ⁴⁶Q.-M. Ma, Z. Xie, J. Wang, Y. Liu, and Y.-C. Li, “Structures, binding energies and magnetic moments of small iron clusters: A study based on all-electron DFT,” *Solid State Communications* **142**, 114–119 (2007).
- ⁴⁷A. Aktürk and A. Sebetci, “BH-DFTB/DFT calculations for iron clusters,” *AIP Advances* **6**, 055103 (2016).
- ⁴⁸K. Cervantes-Salguero and J. M. Seminario, “Structure and energetics of small iron clusters,” *Journal of Molecular Modeling* **18**, 4043–4052 (2012).
- ⁴⁹S. Yu, S. Chen, W. Zhang, L. Yu, and Y. Yin, “Theoretical study of electronic structures and magnetic properties in iron clusters ($n \leq 8$),” *Chemical Physics Letters* **446**, 217–222 (2007).
- ⁵⁰A. P. Thompson, H. M. Aktulga, R. Berger, D. S. Bolintineanu, W. M. Brown, P. S. Crozier, P. J. in ’t Veld, A. Kohlmeyer, S. G. Moore, T. D. Nguyen, R. Shan, M. J. Stevens, J. Tranchida, C. Trott, and S. J. Plimpton, “LAMMPS - a flexible simulation tool for particle-based materials modeling at the atomic, meso, and continuum scales,” *Comp. Phys. Comm.* **271**, 108171 (2022).
- ⁵¹M. W. Finnis and J. E. Sinclair, “A simple empirical N-body potential for transition metals,” *Philosophical Magazine A* **50**, 45–55 (1984).
- ⁵²M. I. Mendeleev, S. Han, D. J. Srolovitz, G. J. Ackland, D. Y. Sun, and M. Asta, “Development of new interatomic potentials appropriate for crystalline and liquid iron,” *Philosophical Magazine* **83**, 3977–3994 (2003).
- ⁵³J. Elliott, Y. Shibuta, and D. Wales, “Global minima of transition metal clusters described by Finnis–Sinclair potentials: A comparison with semi-empirical molecular orbital theory,” *Philosophical Magazine* **89**, 3311–3332 (2009).
- ⁵⁴G. Bussi and M. Parrinello, “Accurate sampling using langevin dynamics,” *Phys. Rev. E* **75**, 056707 (2007).
- ⁵⁵G. A. Breaux, B. Cao, and M. F. Jarrold, “Second-Order Phase Transitions in Amorphous Gallium Clusters,” *The Journal of Physical Chemistry B* **109**, 16575–16578 (2005), publisher: American Chemical Society.
- ⁵⁶D. Gerion, A. Hirt, I. M. L. Billas, A. Châtelain, and W. A. de Heer, “Experimental specific heat of iron, cobalt, and nickel clusters studied in a molecular beam,” *Phys. Rev. B* **62**, 7491–7501 (2000).